Contents lists available at ScienceDirect

European Journal of Mechanics / A Solids

journal homepage: www.elsevier.com/locate/ejmsol

Probing porosity in metals by electrical conductivity: Nanoscale experiments and multiscale simulations

Tobias Kaiser [a,*], Gerhard Dehm [b], Christoph Kirchlechner [c], Andreas Menzel [a,d], Hanna Bishara [b,e]

[a] *Institute of Mechanics, TU Dortmund University, Leonhard-Euler-Str. 5, 44227 Dortmund, Germany*
[b] *Max-Planck-Institut für Eisenforschung GmbH, 40237 Düsseldorf, Germany*
[c] *Institute for Applied Materials, Karlsruhe Institute of Technology, Hermann von Helmholtz Platz 1, 76344 Eggenstein-Leopoldshafen, Germany*
[d] *Division of Solid Mechanics, Lund University, P.O. Box 118, SE-22100 Lund, Sweden*
[e] *Department of Materials Science and Engineering, Tel Aviv University, Ramat Aviv 6997801, Tel Aviv, Israel*

ABSTRACT

Motivated by the significant influence of the underlying microstructure on the effective electrical properties of a material system and the desire to monitor defect evolution through non-destructive electrical characterisation, this contribution is concerned with a detailed study of conductivity changes caused by the presence of sub-microscale pores. Reducing the complexity of the material system, geometrically well-defined pore arrays are created by focused ion beam (FIB) milling in Cu thin films and characterised by 4-point probe electrical measurements. The experiment is designed such that it reduces to a (quasi-)one-dimensional electrical problem which is amenable to analytical techniques when invoking a computational homogenisation scheme to approximate the effective electrical properties of a given microstructure. The applicability of the proposed approach is shown in a first step by comparing simulation results for different pore volume fractions and pore shapes against their experimental counterparts. In a second step, a sensitivity analysis of the experimental data is carried out and the usefulness of the proposed modelling approach in interpreting the experimental data is demonstrated. In particular, the findings suggest that the proposed experimental method allows (at best) the determination of pore volume fractions with an accuracy of $\pm 0.5\%$.

1. Introduction

Electrical properties of materials are significantly affected by their microstructure, e.g. by grain boundaries (Arenas et al., 2015; Gall, 2020; Bishara et al., 2020), cracks (Cordill et al., 2016; Kaiser et al., 2021), or dislocations (Basinski et al., 1963; Muhammad et al., 2022). In classic approaches, the effect of these defects on the conductivity of the material is captured in a cumulative way, without distinguishing the contributions of individual defects. However, understanding the way each defect affects the conductivity allows for better monitoring of defect evolution through non-destructive electrical characterisation. This is, for instance, important for monitoring defect formation during processing in electronic devices, for tracking mechanical deformation such as fatigue in thin films (Kaiser et al., 2021), or for characterising chemical changes due to harsh environments (Stelzer et al., 2020).

In order to estimate the impact of defects on the resistivity of a material, various approaches are used depending on the defect type. For instance, grain boundaries are treated either with analytical or empirical models that consider the density and specific resistivity of the boundaries (Bakonyi, 2021). Cracks in thin films are characterised by using confocal laser scanning microscopy (CLSM) and changes in resistivity of the cyclically-strained samples are studied by means of 4-point probe measurements in Cordil et al. (2017). Regarding pore-type defects, the material's porosity may be characterised by means of electrical measurements. In particular, non-contact electromagnetic field-based measurements (Bakhtiyarov and Overfelt, 2004; He et al., 2018) and 4-point probe measurements (Polder, 2001) are used. The contribution of pores has been shown to depend on their location and orientation (Bakhtiyarov and Overfelt, 2004). Hence, simulations that calculate the resistivity with the mixture rule fail to precisely reproduce the experimental data (Bakhtiyarov and Overfelt, 2004). Alternatively, analytical models for highly porous materials are proposed that relate the porosity to the electrical resistivity and that account for geometrical effects, e.g., by modelling the material in terms of octahedrons (Liu et al., 1999). Moreover, the effect of porosity on conductivity is studied on a lower scale by considering the potential of pores in a quantum

---

theory solution of electrons propagating in the porous media (Martin and Paetsch, 1973). However, reaching acceptable agreement between experimental data and simulation-based predictions on the effect of specific pore geometries and the pore density is still an open challenge, so that a systematic study is required.

Computational multiscale methods are powerful numerical techniques to predict the effective constitutive response of complex materials, possibly featuring multiple phases, inclusions or pores. They are based on the construction of a microscale boundary value problem that allows detailed information on the underlying microstructure to be accounted for, and rely on homogenisation techniques to relate microscale to macroscale fields, (Geers et al., 2010). Originating from the pioneering works (Suquet, 1985; Renard and Marmonier, 1987), these methods are nowadays applied to study purely mechanical (Miehe et al., 1999; Feyel and Chaboche, 2000; Kouznetsova et al., 2001; Ricker et al., 2010; Coenen et al., 2012; Javili et al., 2017), thermo-mechanical (Özdemir et al., 2008; Temizer and Wriggers, 2011; Sengupta et al., 2012; Berthelsen et al., 2017; Berthelsen and Menzel, 2019), acoustic (Gao et al., 2017; Lewińska et al., 2019) and electro-mechanical (Schröder, 2009; Khalaquzzaman et al., 2012; Keip et al., 2014) material behaviour (of dielectrics) across multiple scales. In this regard, the present contribution is based on recent developments on computational multiscale methods for electrical conductors (Kaiser and Menzel, 2021a,b). More specifically speaking, a numerical scheme was elaborated and effective electrical properties of conducting materials featuring pore-type defects were studied in Kaiser and Menzel (2021a). However, the developments were limited to numerical analyses and experimental data was not taken into account.

Against this background, periodic arrays of defects that are similar to the ones studied in Kaiser and Menzel (2021a) are experimentally analysed in this work, and the measured changes in resistance due to the presence of defects are compared against numerical predictions. Although the shape and the distribution of pore-type defects that occur in real materials are certainly more complex than the artificial defects analysed, a significant step is taken in this work towards applying the electrical homogenisation technique to real systems by systematically analysing a model system. The purpose of this contribution is thus two-fold: on the one hand, it contributes to an understanding of experimentally obtained data, eventually allowing the study and separation of different micromechanical processes and phenomena in future works. On the other hand, it demonstrates the applicability of the proposed computational multiscale approach to electrical conductors by comparison with experimental data for representative sample problems. Put into perspective, the fundamental study carried out in the present work thus contributes to the systematic development of non-destructive methods for the characterisation of (mechanically-induced) microscale defects such as cracks and pores. Likewise, by establishing microstructure–property relations, a basis for the development of predictive simulation approaches is provided. By systematically including information from further fundamental studies, e.g. on the influence of the dislocation density or of grain boundaries on the effective electrical conductivity, and by considering established approaches towards the modelling of damage and plasticity this eventually allows for the predictive simulation of evolving microstructures and of their effective electrical properties.

The contribution is structured as follows: Section 2 provides an overview of the experiments, of the computational homogenisation scheme, and of the modelling framework used. Based on these developments, a detailed comparison of experimental results and simulations is carried out in Section 3.1, and the usefulness of the proposed modelling approach in interpreting experimental data is demonstrated in Section 3.2. Concluding remarks are drawn in Section 4.

2. Method

In this study, microstructural units are represented by periodic pores. In order to simplify the system so that it fits experimental and simulation techniques, a two-dimensional thin film material system is considered and the electrical problem is reduced to a (quasi-)one-dimensional one. This is done by isolating an elongated rectangle in a metallic thin film by FIB milling, while the pores are restricted inside the rectangle. By making use of computational homogenisation techniques, the resulting system allows for a (semi-)analytical solution of the electrical field distribution. A description of the methodology and the geometries studied is given below. In particular, the experiments are discussed in Section 2.2, the fundamentals of computational homogenisation approaches are summarised in Section 2.3, and the modelling approach taken is elaborated in Section 2.4.

2.1. Notation

Let α, β, γ, δ denote first order tensors and let $\otimes$ denote the classic dyadic product. With these definitions at hand, the single tensor contraction is introduced as $[\alpha \otimes \beta] \cdot [\gamma \otimes \delta] = [\beta \cdot \gamma] [\alpha \otimes \delta]$. Moreover, (right-)gradient, (right-)divergence and (right-)curl operators are denoted as ∇, $\nabla\cdot$, and $\nabla\times$, respectively.

2.2. Experiments

2.2.1. Thin film deposition

A Cu thin film as a model system that is heavily used in semiconductor industry was deposited on the basal plane of α-Al_2O_3 substrate by magnetron sputtering at room temperature (PVD cluster – Bestec). The deposition was performed at background pressure of 0.66 Pa and 20 sscm Ar flow, with 250 W power supplied by a radio frequency (RF) power generator. A deposition time of 35 min yielded a 500 nm thick film. Post-deposition thermal annealing was carried out at 350 °C for 2 h in the sputtering chamber. The microstructure of the thin film produced in this way was similar to the one reported in Bishara et al. (2021), i.e. a grain size of tens of micrometers and a preferred crystallographic orientation of (111) planes parallel to the surface were observed.

2.2.2. Creation of artificial pores

Pores were created within the thin film by using FIB (Augira, Zeiss) milling through the whole film thickness. Four different geometries of the unit cells were prepared. They are shown in Fig. 1 and the geometric dimensions are provided in Section 3.1 and Fig. 5. To minimise FIB damage (Kiener et al., 2007), a low milling current of 20 pA was used. Arrays of 5×5 repeating units were formed by the program NanoPatterning and Visualization Engine (NPVE). The number of repeated unit cells is limited by the drift of the ion beam during the milling time. When the array exceeded 5×5, a significant beam drift caused distortion of the periodic structure. The array is surrounded by three trenches which constrain the electric current.

2.2.3. Electrical measurements

Electrical measurements of the artificial microstructures are carried out by 4-point probe electrical measurements inside an SEM (Gemini500, Zeiss). Four needles with tip radii of 50 nm, driven by four independent piezoelectric micromanipulators (PS4, Kleindiek), approach the surface of the sample as shown in Fig. 1(a). The outer needles supply the electric current and are in a fixed position during the experiment. The inner needles are used to measure the voltage drop. In particular, the position of one of the needles remains fixed during the experiment, while the other moves along the measurement line towards the outer needle, see Fig. 1(a). Voltage is measured for five different positions of the mobile needle. The initial distance between the needles is 20 μm, which guarantees that the voltage measurement is performed in
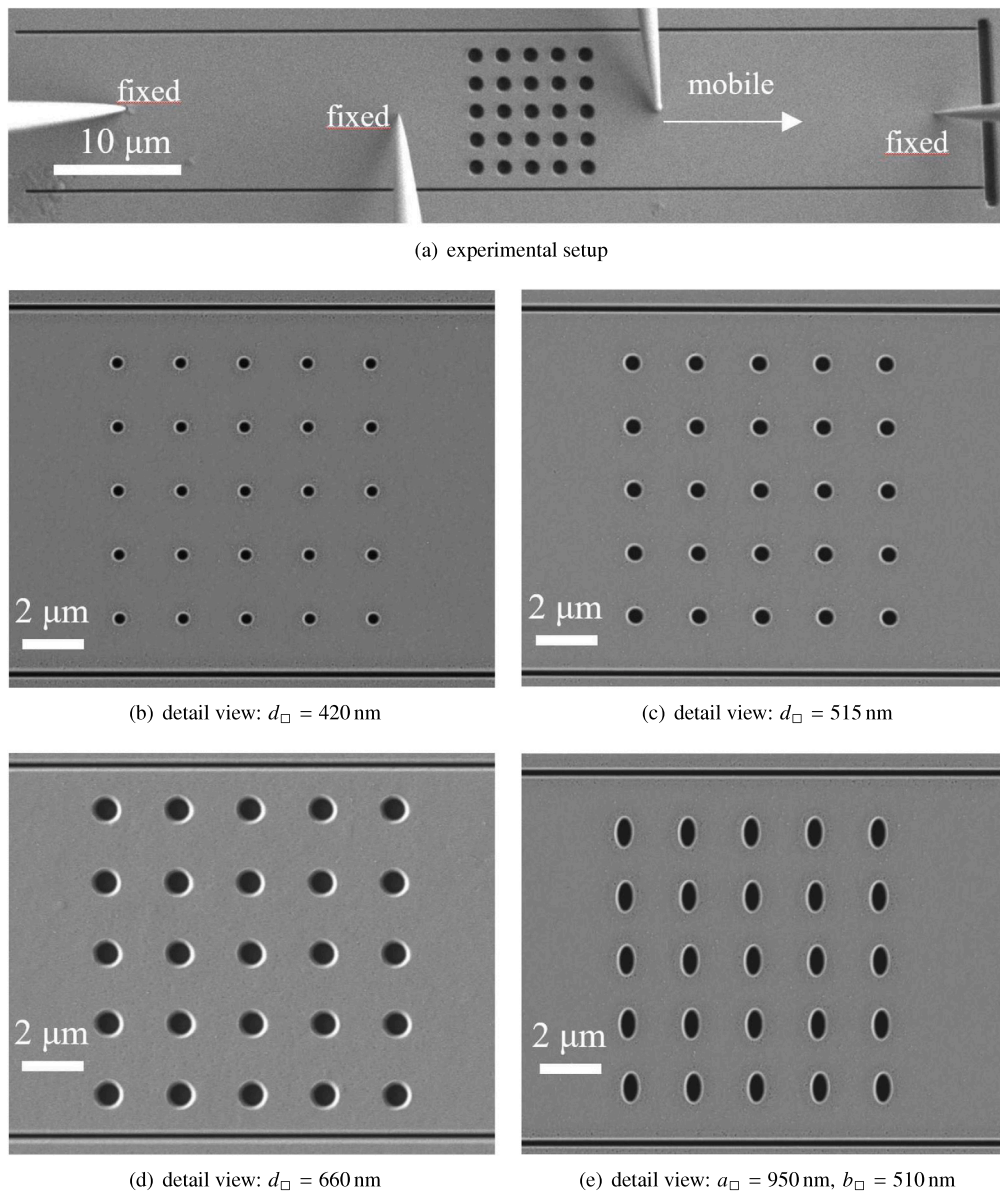
(a) experimental setup

(b) detail view: $d_\square = 420\,\text{nm}$

(c) detail view: $d_\square = 515\,\text{nm}$

(d) detail view: $d_\square = 660\,\text{nm}$

(e) detail view: $a_\square = 950\,\text{nm}$, $b_\square = 510\,\text{nm}$

Fig. 1. Artificially created microstructures featuring circular pores of diameter $d_\square$ and elliptical pores with principal axes $\{a_\square, b_\square\}$, respectively.

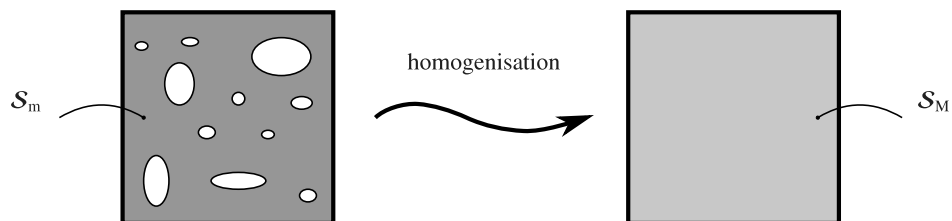**Fig. 2.** Homogenisation of multiphase materials. The effective conductivity tensor $\mathcal{S}_{\text{M}}$ (right) for a unit cell featuring base material and non-conducting pores (left) is calculated.

regions where the electrical field is constant along lines perpendicular to the conduction line (see Remark 1). The non-homogeneous electrical field regions, which are avoided in the measurements, are located at a distance of $\sim 5\,\mu\text{m}$ from the outer needles, and at a minimal distance of $\sim 5\,\mu\text{m}$ from the inner needles. Electrical measurements are conducted by 100 consequent direct current (dc) pulses with magnitude of $10\,\text{mA}$ and width of $10\,\text{ms}$. The pulse technique aims to avoid contact drift issues and increases the reliability of the measurement as described in Bishara et al. (2020). Moreover, it was reported in Bishara et al.

(2020) that a representative value of resistivity of an individual grain boundary is $10^{-15}\,\Omega\,\text{m}^2$. Hence, approximating the grain boundary area by the cross-sectional area of the thin film, i.e. $500\,\text{nm}$ thickness and $10\,\mu\text{m}$ length (height of the milled structure), and evaluating Ohm's law for a $10\,\text{mA}$ current yields a voltage change in the order of μV per grain boundary, which is below the error bar oft the measurement. Given that there are, on average, only one or two grain boundaries in the measured area, the grain boundary effect on the measured potential difference is assumed to be negligible for the present study.
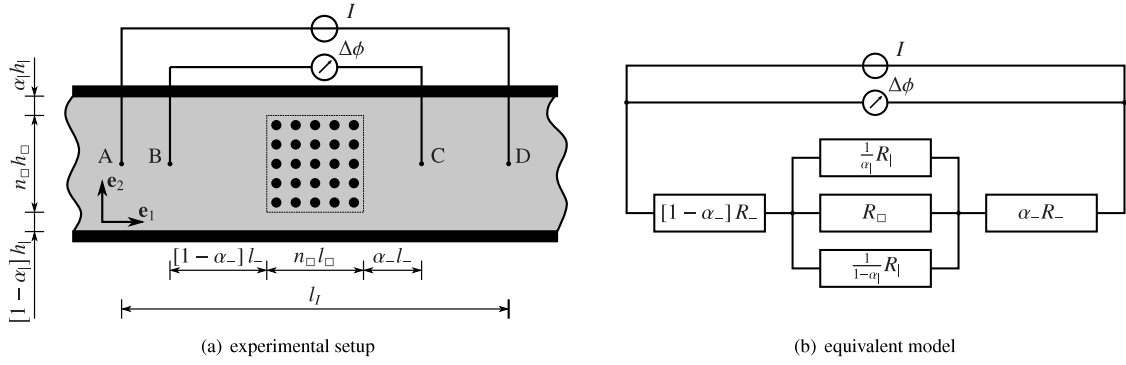
(a) experimental setup

(b) equivalent model

Fig. 3. Experimental setup and modelling approach with $0 \leq \alpha_- \leq 1$, $0 \leq \alpha_| \leq 1$ and $l_\phi = n_\square l_\square + l_-$. The material and structural properties do not significantly vary over the thickness t, such that a two-dimensional modelling approach is taken.

2.3. Computational homogenisation

To calculate (effective) homogenised material properties for specific microstructures, a particularised version of the computational homogenisation scheme discussed in Kaiser and Menzel (2021a) is used. More specifically speaking, by restricting the model to quasi-stationary electric problems, the governing set of balance equations reduces to the continuity equation

$$\nabla \cdot \boldsymbol{j} = 0 \tag{1}$$

and to the Maxwell–Faraday equation with a vanishing induction term

$$\nabla \times \boldsymbol{e} = \boldsymbol{0} \quad . \tag{2}$$

Whereas the latter balance equation can a priori be fulfilled by the introduction of an electric potential field ϕ which is related to the electric field vector $\boldsymbol{e}$ via

$$\boldsymbol{e} = -\nabla \phi \quad , \tag{3}$$

the former balance equation requires constitutive relations for electric current density vector $\boldsymbol{j}$ to be postulated in accordance with the restrictions posed by the second law of thermodynamics. For the sake of simplicity, the linear relation

$$\boldsymbol{j}_\text{m} = \boldsymbol{S}_\text{m} \cdot \boldsymbol{e}_\text{m} \tag{4}$$

between the electric current density vector and the electric field vector is assumed at each microscale material point. Moreover, the particular choice for the positive (semi-)definite conductivity tensor

$$\boldsymbol{S}_\text{m} = \kappa \, \boldsymbol{I} \quad , \tag{5}$$

with κ denoting a scalar-valued material parameter and $\boldsymbol{I}$ the second order identity tensor, results in an isotropic microscale material response.

Based on a detailed representation of the underlying material microstructure, (effective) homogenised conductivity (or rather tangent stiffness) tensors can be calculated for inhomogeneous microstructures, see Fig. 2. More specifically speaking, these tensors can be condensed from the microscale boundary value problems and can be shown to take the form

$$\boldsymbol{S}_\text{M} = \frac{\text{d}\boldsymbol{j}_\text{M}}{\text{d}\boldsymbol{e}_\text{M}} = -\frac{1}{v_\text{m}} \sum_{i=1}^{n_\text{pn}} \sum_{j=1}^{n_\text{pn}} {}^{(ij)}\widehat{\mathbf{K}}_\text{m}^{\phi\phi} \, {}^{(i)}\boldsymbol{x}_\text{m} \otimes {}^{(j)}\boldsymbol{x}_\text{m} \tag{6}$$

for linear and periodic boundary conditions, where v_m denotes the total volume of and $\boldsymbol{x}_\text{m}$ the position in the unit cell, n_pn specifies the number of nodes where the electric potential is prescribed and ${}^{(ij)}\widehat{\mathbf{K}}_\text{m}^{\phi\phi}$ is a sub-matrix of the generalised stiffness matrix that results from the finite element discretisation of the microstructure, cf. (Kaiser and Menzel, 2021a, (62)). It is noted that $\boldsymbol{S}_\text{M}$ would not be constant but state-dependent if a non-linear constitutive relation was adopted in (4).

2.4. Modelling approach

The experiments are designed such that an overall quasi-unidirectional electric current is observed that is, however, strongly inhomogeneous in the region where the microstructural imperfections are induced. Motivated by Saint-Venant's principle of mechanical problems, it is thus proposed to measure the electric potential difference at a distance from the imperfections and to evaluate their influence on the overall electrical material properties by using the equivalent model sketched in Fig. 3.

More specifically speaking, the electric potential difference $\Delta\phi$ between the points B and C that are a distance $l_\phi < l_I$ apart is in a first step measured for a prescribed electric current I. In a second step, the experimental data is compared with simulation results that are based on series and parallel connections of resistors as sketched out in Fig. 3(b). In addition to the effective resistance $R_\square$ associated with the $n_\square \times n_\square$ array of unit cells, the resistance caused by the material region of length l_-, i.e. R_-, and the resistance associated with the material region of height $h_|$, i.e. $R_|$, are accounted for. In this regard, it is noted that the geometric dimensions are directly extracted from the experimental images. The remaining unknowns that occur in the calculation of the potential difference

$$
\begin{aligned}
\Delta\phi\left(l_\phi\right) &\approx \left[R_- + \left[\frac{1}{R_\square} + \frac{1}{R_|}\right]^{-1}\right] I \\
&= \left[\frac{1}{\kappa}\frac{l_\phi - n_\square l_\square}{[h_| + n_\square h_\square]\, t} + \left[\kappa_\square \frac{h_\square t}{l_\square} + \kappa \frac{h_| t}{n_\square l_\square}\right]^{-1}\right] I
\end{aligned}
\tag{7}
$$

are the scalar-valued conductivity κ of the base material, and the effective conductivity (in $\boldsymbol{e}_1$-direction) of the material region that features pores, $\kappa_\square$. Conductivity coefficient $\kappa_\square$ is, however, not independent but can be related to the conductivity of the base material by making use of the computational homogenisation scheme presented in Section 2.3 and by projecting the homogenised conductivity tensor $\boldsymbol{S}_\text{M}$ into the $\boldsymbol{e}_1$-direction,

$$\kappa_\square = \boldsymbol{e}_1 \cdot \boldsymbol{S}_\text{M} \cdot \boldsymbol{e}_1 \quad . \tag{8}$$

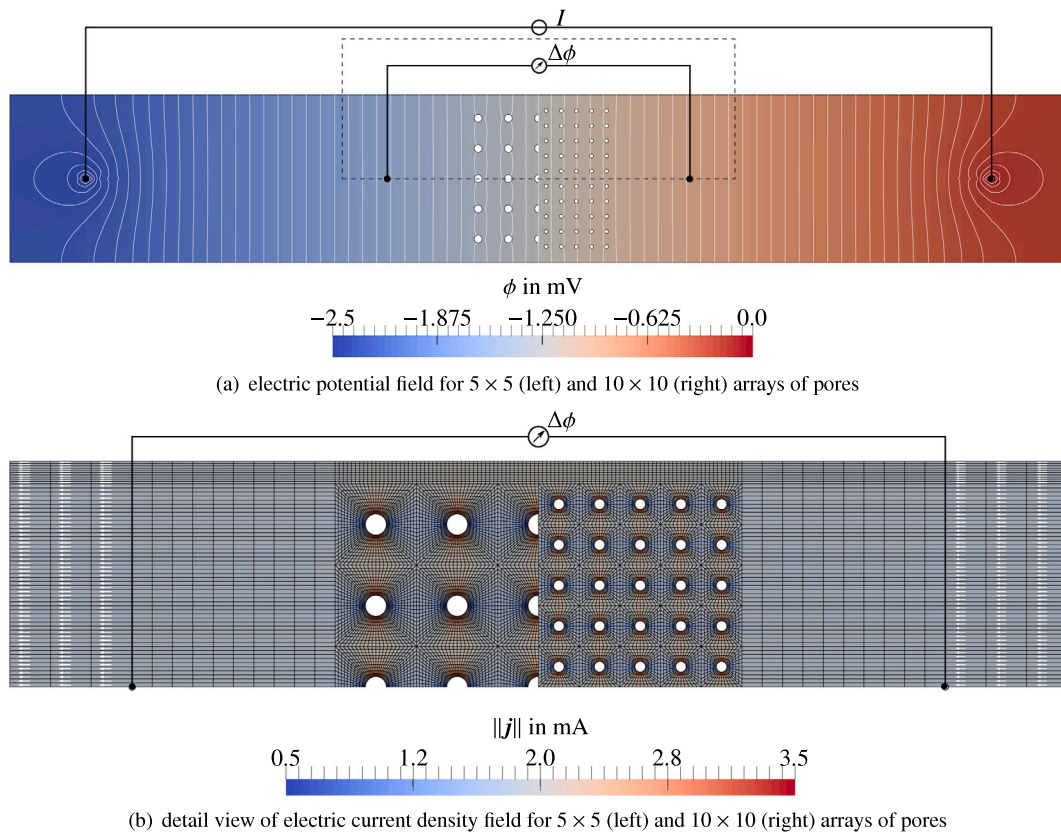Accordingly, by making use of the computational homogenisation scheme and by introducing the conductivity ratio

$$\beta_\square = \kappa_\square / \kappa \tag{9}$$

that measures the influence of the pore-type inclusions on the effective resistivity, relation (7) can be recast in the form

$$\Delta\phi\left(l_\phi\right) \approx \left[\frac{l_\phi - n_\square l_\square}{[h_| + n_\square h_\square]\, t} + \left[\beta_\square \frac{h_\square t}{l_\square} + \frac{h_| t}{n_\square l_\square}\right]^{-1}\right] \frac{I}{\kappa} \quad . \tag{10}$$

Remark 1 (*Separation of scales and boundary effects*). With regard to the experiments and the modelling approach taken, the following

(a) electric potential field for 5×5 (left) and 10×10 (right) arrays of pores

(b) detail view of electric current density field for 5×5 (left) and 10×10 (right) arrays of pores

Fig. 4. Electric potential field ϕ and electric current density field j, respectively $\|j\| = \sqrt{j \cdot j}$, for simulations with fully resolved microstructures – 5×5 and 10×10 arrays of pores with diameters $d_\square = 515$ nm and $d_\square = 257.5$ nm are considered. Simulation results are provided for a prescribed electric current $I = 10$ mA, isolines are shown in a), and electric current density vectors at a distance from the pores are indicated by small white-coloured arrows in b). The isolines and the current density vectors reveal the homogeneity of the fields at a distance from the pores. For presentation purposes half of the boundary value problem is depicted in a) for each geometry studied and a detail view on the centre area (marked by dashed-lines in a)) is provided in b).

questions naturally arise: (1) The derivation of the equivalent model in Section 2.4 is based on the assumption of a quasi-one-dimensional setting. However, the fields are strongly inhomogeneous in the centre region of the specimen and near the contact points of the outer needles. The potential influence of these inhomogeneities on the experimentally recorded data and on the simulation results needs to be analysed. (2) Computational multiscale approaches intrinsically rely on a 'sufficient' separation of scales. The characteristic length of the macroscale, i.e. the height of the sample, is approximately 10 μm. The characteristic length of the microscale features, i.e. of the pores, ranges between 0.42 μm and 0.95 μm. The rather moderate separation of length scales and its potential influence on the simulation results thus needs to be assessed.

In order to address these questions, macroscale simulations with fully resolved microstructures that feature 5×5 and 10×10 arrays of pores with diameters $d_\square = 515$ nm and $d_\square = 257.5$ nm are exemplarily considered, see Fig. 4. Regarding the former sample geometry, which is used in the experiments, it is observed that the fields are homogeneous at a distance from the centre region and from the contact points, respectively, and that the disturbances decrease quickly. Moreover, the difference in the $\Delta\phi-l_\phi$-curves (Fig. 6(a)) between the homogenisation-based modelling approach and the two macroscale simulations with resolved microstructures that feature the same pore volume fractions is almost negligible – specifically speaking, a maximal difference in $\Delta\phi$ for $l_\phi \in [19 \,\mu m, 27 \,\mu m]$ of approximately 6.2×10^{-4} mV is found between the three different simulation approaches.

3. Experimental findings and simulation results

In this section, the modelling approach proposed in Section 2.4 is first applied to representative microstructures to show its applicability

before a sensitivity analysis of the experimental data is carried out and the usefulness of the proposed approach in interpreting experimental data is demonstrated.

3.1. Comparison of experiment and simulation

To study the applicability of the computational homogenisation scheme discussed in Section 2.3, the finite element discretised unit cells shown in Fig. 5 were, in a first step, prepared from the experimental images shown in Fig. 1. Based on these, the effective conductivity tensors and conductivity ratios, namely,

$$[S_M]_{ij}^{d420} = \begin{bmatrix} 0.9332 & 0.0000 \\ 0.0000 & 0.9332 \end{bmatrix} \kappa \quad , \quad \beta_\square^{d420} = 0.9332 \tag{11a}$$

$$[S_M]_{ij}^{d515} = \begin{bmatrix} 0.9012 & 0.0000 \\ 0.0000 & 0.9012 \end{bmatrix} \kappa \quad , \quad \beta_\square^{d515} = 0.9012 \tag{11b}$$

$$[S_M]_{ij}^{d660} = \begin{bmatrix} 0.8426 & 0.0000 \\ 0.0000 & 0.8426 \end{bmatrix} \kappa \quad , \quad \beta_\square^{d660} = 0.8426 \tag{11c}$$

$$[S_M]_{ij}^{elli} = \begin{bmatrix} 0.7589 & 0.0000 \\ 0.0000 & 0.8644 \end{bmatrix} \kappa \quad , \quad \beta_\square^{elli} = 0.7589 \tag{11d}$$

were calculated in a second step by application of the computational homogenisation scheme with periodic boundary conditions. Taking a closer look at the conductivity tensors it shows that, as expected, circular pores give rise to isotropic conductivity tensors with a reduced effective conductivity, whereas elliptic pores manifest themselves in an anisotropic material response. For the proposed experimental setup, the principal axes of S_M^{elli} are, however, still aligned with the $\mathbf{e}_1$- and $\mathbf{e}_2$-coordinate axes.

(a) $d_\square = 420\,\text{nm}$

(b) $d_\square = 515\,\text{nm}$

(c) $d_\square = 660\,\text{nm}$

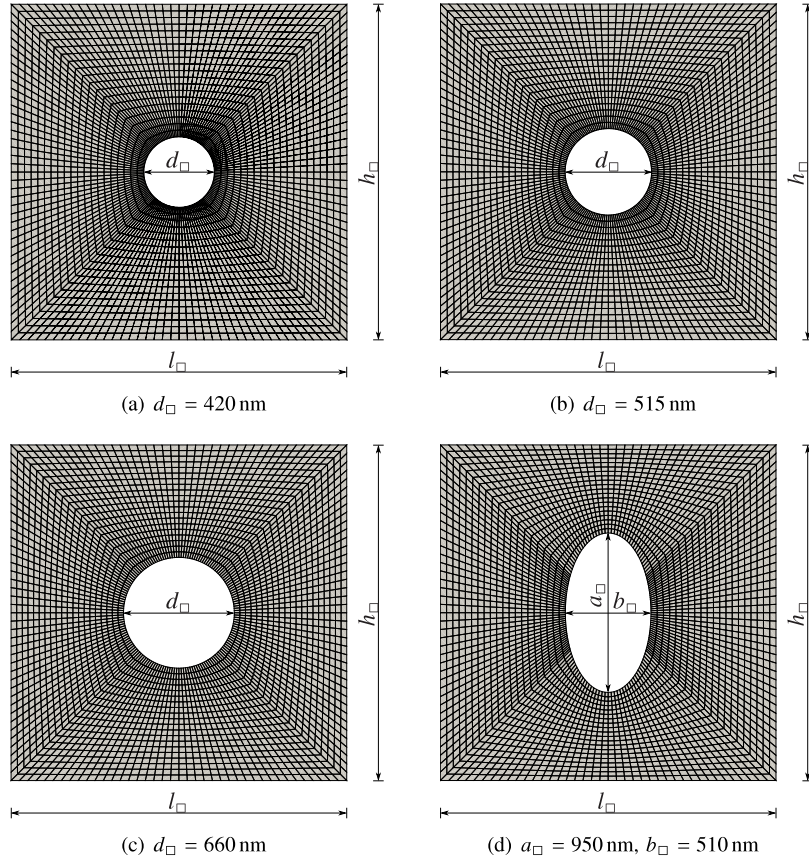(d) $a_\square = 950\,\text{nm}$, $b_\square = 510\,\text{nm}$

Fig. 5. Finite element discretised unit cells with $l_\square = h_\square = 2000\,\text{nm}$.

Table 1
Relation between pore volume fraction $\eta_\square$ and conductivity ratio $\beta_\square$ for circular pores.

$\eta_\square$	0.00%	0.20%	0.79%	1.77%	3.14%	4.91%	7.07%	9.62%	12.57%
$\beta_\square$	1.000	0.996	0.985	0.965	0.939	0.907	0.868	0.825	0.777

In addition to the microstructures with pores sketched in Fig. 5, an ideal Cu thin film is taken into account as a reference. For all samples, a spatially uniform thickness $t = 500\,\text{nm}$ is assumed and the geometric dimensions $h_|^{\text{blank}} = 1.50\,\mu\text{m}$, $h_|^{\text{d420}} = 1.22\,\mu\text{m}$, $h_|^{\text{d515}} = 1.11\,\mu\text{m}$, $h_|^{\text{d660}} = 0.15\,\mu\text{m}$, $h_|^{\text{elli}} = 1.30\,\mu\text{m}$ are extracted from the experimental images by considering the additive split of the total measured height, i.e. $h_| + n_\square h_\square$. With these data at hand and for the particular choice $\kappa = 51.3\,\text{mA/mV}\mu\text{m}$ that is based on the direct measurement of the pristine thin-film, the evaluation of (10) yields the $\Delta\phi - l_\phi$-curves depicted in Fig. 6(a).

In addition, the experimentally obtained data points are provided in Fig. 6(a). As expected, it is observed that the measured voltage-drop between the inner needles increases with the distance between the contacts and that the measured voltage-drop scales with the dimensions of the pores. Overall, experiment and simulation agree well, both quantitatively and qualitatively, which shows both: the accuracy of the electrical measurements and the applicability of the proposed modelling approach.

3.2. Interpretation of experimental data and sensitivity analysis

This section deals with the sensitivity analysis of the experimental data and demonstrates how the proposed framework and, in particular, the simulation results can be used to interpret the experiments.

To this end, the theoretical potential difference according to (7) that is encountered in an idealised experiment ($h_| = 0.00\,\mu\text{m}$) for a material without pores ($d_\square = 0.00\,\text{nm}$),

$$\widetilde{\Delta\phi}\left(l_\phi\right) = \frac{1}{\kappa}\frac{l_\phi}{n_\square h_\square t}\,I \quad , \tag{12}$$

is taken into account as a reference. In a second step, the simulation results for imperfect experiments ($h_| > 0.00\,\mu\text{m}$) with height ratios
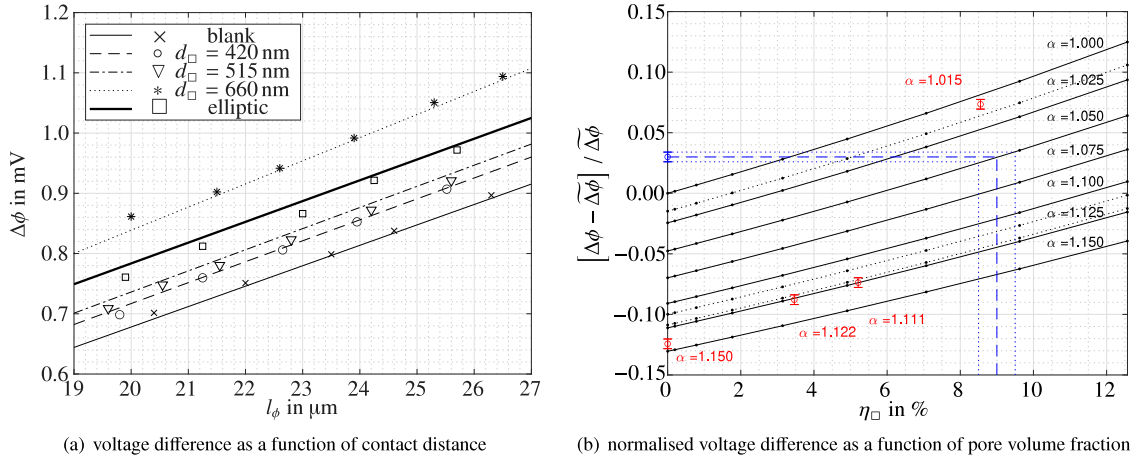
$$\alpha = \frac{n_\square h_\square + h_|}{n_\square h_\square} \tag{13}$$

measuring the deviation of the actual geometry from the assumed ideal geometry, are normalised with respect to $\widetilde{\Delta\phi}\left(l_\phi\right)$ according to

$$\frac{\Delta\phi\left(l_\phi\right) - \widetilde{\Delta\phi}\left(l_\phi\right)}{\widetilde{\Delta\phi}\left(l_\phi\right)} = \frac{1}{\alpha} + \frac{n_\square l_\square}{l_\phi}\left[-\frac{1}{\alpha} + \frac{1}{\alpha + \beta_\square - 1}\right] - 1 \quad , \tag{14}$$

$$l_\phi \geq n_\square l_\square \quad .$$

Following the same lines for the experimentally obtained data points, and evaluating relation (14) at $l_\phi = 23\,\mu\text{m}$ gives rise to the normalised potential difference curves shown in Fig. 6(b). Since samples with the same pore volume fraction but different pore diameters are expected to yield the same overall potential difference $\Delta\phi\left(l_\phi\right)$, cf. Remark 1, the

(a) voltage difference as a function of contact distance

(b) normalised voltage difference as a function of pore volume fraction

Fig. 6. Comparison of experiment and simulation. Simulation results for $I = 10\,\text{mA}$ and $\kappa = 51.3\,\text{mA/mV}\mu\text{m}$ are shown. (a) Experimentally determined ($\times, \circ, \triangledown, *, \square$) and simulated ($-, --, -\cdot-, \cdot\cdot, -$) potential difference as a function of contact distance. (b) Normalised potential difference at contact distance $l_\phi = 23\,\mu\text{m}$ for circular pores with different diameters. Experimental data points are shown with the experimental $0.4\%\ \widetilde{\Delta\phi}$ error bars. Predictions from simulations according to (14) are provided for samples with different height ratios (-). In addition, predictions for height ratios $\alpha \in \{1.015, 1.111, 1.122\}$ (--) that correspond to the experimental data points with pore volume fractions $\eta_\square \in \{8.6\%, 5.2\%, 3.5\%\}$ are provided.

results are presented as a function of the pore volume fraction

$$\eta_\square = \frac{\pi\, d_\square^2}{4\, l_\square\, h_\square} \tag{15}$$

that can be related to conductivity ratio $\beta_\square$ according to Table 1. Moreover, it is noted that, in order to approximate the experimental data at position l_ϕ, a linear regression line was calculated for each pore volume fraction by minimising the least square error between the regression line and the data points.

The experimental results for different pore geometries shown in Fig. 6(a) cannot directly be compared because the distance between unit cells and the longitudinal trenches, $h_|$, varies between the experiments due to FIB-drift constraints, see Fig. 3(a). In essence, this creates a situation which is closer to a non-ideal material system. To describe the deviation from an ideal one-dimensional problem where the trenches are located exactly at the edge of the repeating unit cells such that $h_| = 0.0\,\mu\text{m}$, holds, parameter α is introduced. This parameter is most important for the interpretation of the experiment and, in particular, for evaluating the influence of the pore volume fraction on the resistivity of the material system under consideration. In this regard, it is noticed that the uppermost line in Fig. 6(a) that corresponds to the situation of an idealised experiment ($\alpha = 1.0$) does not reproduce the experimental data. However, when considering the actual geometries, i.e. parameters $\alpha \neq 1.0$, the measured data is almost perfectly reproduced by the simulations.

The preceding analysis suggests that the sensitivity of the method to detect the porosity of the material initially depends on the ability to precisely characterise the geometry. Provided that the deviation from an idealised experiment can be estimated ($\alpha \neq 1.0$) and when considering statistically representative regular arrays of circular pores, the error in the electrical measurements of 0.4% allows a determination of the pore volume fraction with $\sim \pm 0.5\%$ accuracy. This is exemplified in Fig. 6(b) by means of the fictitious blue-coloured experimental data point. Accordingly, the smallest detectable pore diameter for the considered experiment with unit cells of edge length $l_\square = h_\square = 2\,\mu\text{m}$ is $d_\square \approx 160\,\text{nm}$.

4. Conclusions

Changes in the material microstructure, e.g. in terms of morphology, phase composition, and defects manifest themselves in the overall electrical properties of material systems. By applying non-destructive electrical characterisation methods these changes can be monitored in experiments. However, given the complexity of (the processes in) real material systems, the interpretation of experimental data is not trivial. Gaining a detailed understanding of each individual effect that contributes to and developing computational tools to predict changes in the measured electrical signals, is thus an essential step in the development of non-destructive characterisation methods.

With this background in mind, this contribution dealt with a fundamental study of changes in electrical resistivity caused by the presence of sub-microscale pores. In particular, a semi-analytical modelling approach to predict the pore content was proposed. At the outset of the developments, focus was laid on Cu thin films. By applying FIB milling, pore arrays with pre-defined pore geometries, pore volume fractions and pore spacings were artificially generated and characterised by 4-point probe electrical measurements. In addition, the electric current was constrained by introducing trenches into the sample such that the electrical boundary value problem reduced to a (quasi-)one-dimensional one. The reduction in the complexity of the problem was the key for the subsequent systematic comparison of experimental results and simulation-based predictions. In particular, the pores were geometrically resolved in terms of unit-cells and their influence on the effective conductivity was determined by applying computational homogenisation techniques. With the effective conductivity tensors at hand, an analytical estimate for the experimentally determined increase in potential difference due to the presence of pores was derived.

In order to validate the proposed modelling approach, pores of different shape and size were experimentally characterised in a first step. It was shown that a single modelling parameter, i.e. the conductivity of the bulk material, was sufficient to accurately predict the experimentally determined potential differences. In a second step, a sensitivity analysis of the experimental data was carried out, and the proposed modelling approach was applied to study the experimental limits. In particular, it was shown that the pore volume fraction under the assumption of circular pores can (at best) be determined up to $\sim \pm 0.5\%$ with the studied potential difference-based characterisation method.

Follow-up works will provide a detailed discussion on the pore geometry and the pore distribution. Moreover, different defects such as the dislocation density, and grain and phase boundaries in polycrystalline and multiphase materials will be considered. With such a systematically developed modelling approach at hand, the individual contributions of different microscale features to the overall resistivity of a sample may be distinguished. In particular, the collection of microscale features in unit cells will eventually enable detailed analyses of

complex material systems with spatially non-homogeneous properties by means of computational multiscale methods. By combining such an experimentally validated framework with well-established approaches towards the modelling of damage, plasticity, phase transformations and recrystallisation, predictive simulations of deformation-induced changes in the effective conductivity of electronic devices may be carried out. This is not only important for the development of non-destructive characterisation methods but also for the optimisation of manufacturing processes for and the design of electronic components.

CRediT authorship contribution statement

Tobias Kaiser: Conceptualization, Data curation, Formal analysis, Funding acquisition, Investigation, Methodology, Project administration, Resources, Software, Supervision, Validation, Visualization, Writing – original draft, Writing – review & editing. **Gerhard Dehm:** Conceptualization, Formal analysis, Funding acquisition, Methodology, Project administration, Resources, Supervision, Validation, Writing – review & editing. **Christoph Kirchlechner:** Conceptualization, Formal analysis, Funding acquisition, Methodology, Project administration, Resources, Validation, Writing – review & editing. **Andreas Menzel:** Conceptualization, Formal analysis, Funding acquisition, Methodology, Project administration, Resources, Software, Supervision, Validation, Writing – review & editing. **Hanna Bishara:** Conceptualization, Data curation, Formal analysis, Funding acquisition, Investigation, Methodology, Project administration, Resources, Validation, Visualization, Writing – original draft, Writing – review & editing.

Declaration of competing interest

The authors declare that they have no known competing financial interests or personal relationships that could have appeared to influence the work reported in this paper.

Data availability

Data will be made available on request.

Acknowledgements

References

Arenas, C., Henriquez, R., Moraga, L., Muñoz, E., Munoz, R.C., 2015. The effect of electron scattering from disordered grain boundaries on the resistivity of metallic nanostructures. Appl. Surf. Sci. 329, 184–196. http://dx.doi.org/10.1016/j.apsusc.2014.12.045.

Bakhtiyarov, S.I., Overfelt, R.A., 2004. Effect of porosity and metallic insertions on electrical resistivity of A2011 aluminium alloy. Mater. Sci. Technol. 20 (6), 790–794. http://dx.doi.org/10.1179/026708304225016752.

Bakonyi, I., 2021. Accounting for the resistivity contribution of grain boundaries in metals: critical analysis of reported experimental and theoretical data for Ni and Cu. Eur. Phys. J. Plus 136 (4), 410. http://dx.doi.org/10.1140/epjp/s13360-021-01303-4.

Basinski, Z.S., Dugdale, J.S., Howie, A., 1963. The electrical resistivity of dislocations. Phil. Mag. 8 (96), 1989–1997. http://dx.doi.org/10.1080/14786436308209092.

Berthelsen, R., Denzer, R., Oppermann, P., Menzel, A., 2017. Computational homogenisation for thermoviscoplasticity: Application to thermally sprayed coatings. Comput. Mech. 60 (5), 739–766. http://dx.doi.org/10.1007/s00466-017-1436-x.

Berthelsen, R., Menzel, A., 2019. Computational homogenisation of thermo-viscoplastic composites: Large strain formulation and weak micro-periodicity. Comput. Methods Appl. Mech. Engrg. 348, 575–603. http://dx.doi.org/10.1016/j.cma.2018.12.032.

Bishara, H., Ghidelli, M., Dehm, G., 2020. Approaches to measure the resistivity of grain boundaries in metals with high sensitivity and spatial resolution: A case study employing Cu. ACS Appl. Electron. Mater. 2 (7), 2049–2056. http://dx.doi.org/10.1021/acsaelm.0c00311.

Bishara, H., Lee, S., Brink, T., Ghidelli, M., Dehm, G., 2021. Understanding grain boundary electrical resistivity in Cu: The effect of boundary structure. ACS Nano 15 (10), 16607–16615. http://dx.doi.org/10.1021/acsnano.1c06367.

Coenen, E.W.C., Kouznetsova, V.G., Bosco, E., Geers, M.G.D., 2012. A multi-scale approach to bridge microscale damage and macroscale failure: a nested computational homogenization-localization framework. Int. J. Fract. 178, 157–178. http://dx.doi.org/10.1007/s10704-012-9765-4.

Cordill, M.J., Glushko, O., Kleinbichler, A., Putz, B., Többens, D.M., Kirchlechner, C., 2017. Microstructural influence on the cyclic electro-mechanical behaviour of ductile films on polymer substrates. Thin Solid Films 644, 166–172. http://dx.doi.org/10.1016/j.tsf.2017.06.067.

Cordill, M.J., Glushko, O., Putz, B., 2016. Electro-mechanical testing of conductive materials used in flexible electronics. Front. Mater. 3, 1–11. http://dx.doi.org/10.3389/fmats.2016.00011.

Feyel, F., Chaboche, J.-L., 2000. FE^2 multiscale approach for modelling the elasto-viscoplastic behaviour of long fibre SiC/Ti composite materials. Comput. Methods Appl. Mech. Engrg. 183 (3), 309–330. http://dx.doi.org/10.1016/S0045-7825(99)00224-8.

Gall, D., 2020. The search for the most conductive metal for narrow interconnect lines. J. Appl. Phys. 127 (5), 050901. http://dx.doi.org/10.1063/1.5133671.

Gao, K., van Dommelen, J.A.W., Geers, M.G.D., 2017. Investigation of the effects of the microstructure on the sound absorption performance of polymer foams using a computational homogenization approach. Eur. J. Mech. A Solids 61, 330–344. http://dx.doi.org/10.1016/j.euromechsol.2016.10.011.

Geers, M.G., Kouznetsova, V.G., Brekelmans, W.A.M., 2010. Multi-scale computational homogenization: Trends and challenges. J. Comput. Appl. Math. 234 (7), 2175–2182. http://dx.doi.org/10.1016/j.cam.2009.08.077.

He, R., Ma, H., Hafiz, R.B., Fu, C., Jin, X., He, J., 2018. Determining porosity and pore network connectivity of cement-based materials by a modified non-contact electrical resistivity measurement: Experiment and theory. Mater. Des. 156, 82–92. http://dx.doi.org/10.1016/j.matdes.2018.06.045.

Javili, A., Steinmann, P., Mosler, J., 2017. Micro-to-macro transition accounting for general imperfect interfaces. Comput. Methods Appl. Mech. Engrg. 317, 274–317. http://dx.doi.org/10.1016/j.cma.2016.12.025.

Kaiser, T., Cordill, M.J., Kirchlechner, C., Menzel, A., 2021. Electrical and mechanical behaviour of metal thin films with deformation-induced cracks predicted by computational homogenisation. Int. J. Fract. 231 (2), 223–242. http://dx.doi.org/10.1007/s10704-021-00582-3.

Kaiser, T., Menzel, A., 2021a. An electro-mechanically coupled computational multiscale formulation for electrical conductors. Arch. Appl. Mech. 91, 1509–1526. http://dx.doi.org/10.1007/s00419-020-01837-6.

Kaiser, T., Menzel, A., 2021b. A finite deformation electro-mechanically coupled computational multiscale formulation for electrical conductors. Acta Mech. 232, 3939–3956. http://dx.doi.org/10.1007/s00707-021-03005-5.

Keip, M.-A., Steinmann, P., Schröder, J., 2014. Two-scale computational homogenization of electro-elasticity at finite strains. Comput. Methods Appl. Mech. Engrg. 278, 62–79. http://dx.doi.org/10.1016/j.cma.2014.04.020.

Khalaquzzaman, M., Xu, B.-X., Ricker, S., Müller, R., 2012. Computational homogenization of piezoelectric materials using FE2 to determine configurational forces. Technische Mechanik 32 (1), 21–37.

Kiener, D., Motz, C., Rester, M., Jenko, M., Dehm, G., 2007. FIB damage of Cu and possible consequences for miniaturized mechanical tests. Mater. Sci. Eng. A 459 (1), 262–272. http://dx.doi.org/10.1016/j.msea.2007.01.046.

Kouznetsova, V.G., Brekelmans, W.A.M., Baaijens, F.P.T., 2001. An approach to micro-macro modeling of heterogeneous materials. Comput. Mech. 27 (1), 37–48. http://dx.doi.org/10.1007/s004660000212.

Lewińska, M.A., Kouznetsova, V.G., van Dommelen, J.A.W., Geers, M.G.D., 2019. Computational homogenisation of acoustic metafoams. Eur. J. Mech. A Solids 77, 103805. http://dx.doi.org/10.1016/j.euromechsol.2019.103805.

Liu, P.S., Li, T.F., Fu, C., 1999. Relationship between electrical resistivity and porosity for porous metals. Mater. Sci. Eng. A 268 (1), 208–215. http://dx.doi.org/10.1016/S0921-5093(99)00073-8.

Martin, J.W., Paetsch, R., 1973. Electrical resistivity of voids. J. Phys. F: Metal Phys. 3 (5), 907–917. http://dx.doi.org/10.1088/0305-4608/3/5/005.

Miehe, C., Schotte, J., Schröder, J., 1999. Computational micro-macro transitions and overall moduli in the analysis of polycrystals at large strains. Comput. Mater. Sci. 16 (1), 372–382. http://dx.doi.org/10.1016/S0927-0256(99)00080-4.

Muhammad, Q.K., Bishara, H., Porz, L., Dietz, C., Ghidelli, M., Dehm, G., Frömling, T., 2022. Dislocation-mediated electronic conductivity in rutile. Mater. Today Nano 17, 100171. http://dx.doi.org/10.1016/j.mtnano.2021.100171.

Özdemir, I., Brekelmans, W.A.M., Geers, M.G.D., 2008. FE^2 computational homogenization for the thermo-mechanical analysis of heterogeneous solids. Comput. Methods Appl. Mech. Engrg. 198 (3), 602–613. http://dx.doi.org/10.1016/j.cma.2008.09.008.

Polder, R.B., 2001. Test methods for on site measurement of resistivity of concrete – a RILEM TC-154 technical recommendation. Constr. Build. Mater. 15 (2), 125–131. http://dx.doi.org/10.1016/S0950-0618(00)00061-1.

Renard, J., Marmonier, M.F., 1987. Etude de l'initiation de l'endommagement dans la matrice d'un matériau composite par une méthode d'homogénéisation. Aerosp. Sci. Technol. (6), 43–51.

Ricker, S., Mergheim, J., Steinmann, P., Müller, R., 2010. A comparison of different approaches in the multi-scale computation of configurational forces. Int. J. Fract. 166, 203–214. http://dx.doi.org/10.1007/s10704-010-9525-2.

Schröder, J., 2009. Derivation of the localization and homogenization conditions for electro-mechanically coupled problems. Comput. Mater. Sci. 46 (3), 595–599. http://dx.doi.org/10.1016/j.commatsci.2009.03.035.

Sengupta, A., Papadopoulos, P., Taylor, R.L., 2012. A multiscale finite element method for modeling fully coupled thermomechanical problems in solids. Internat. J. Numer. Methods Engrg. 91 (13), 1386–1405. http://dx.doi.org/10.1002/nme.4320.

Stelzer, B., Momma, M., Schneider, J.M., 2020. Autonomously self-reporting hard coatings: Tracking the temporal oxidation behavior of TiN by in situ sheet resistance measurements. Adv. Funct. Mater. 30 (13), 2000146. http://dx.doi.org/10.1002/adfm.202000146.

Suquet, P.M., 1985. Local and global aspects in the mathematical theory of plasticity. In: Sawczuck, A., Bianchi, G. (Eds.), Plasticity Today: Modelling, Methods and Applications. Springer Netherlands, Dordrecht, pp. 279–310.

Temizer, İ., Wriggers, P., 2011. Homogenization in finite thermoelasticity. J. Mech. Phys. Solids 59 (2), 344–372. http://dx.doi.org/10.1016/j.jmps.2010.10.004.